doi:10.26443/seismica.v2i2.498

Inferring rock strength and fault activation from high-resolution *in situ* V_p/V_s estimates surrounding induced earthquake clusters

M.P. Roth * [1], **A. Verdecchia** [1], **R.M. Harrington** [1], **Y. Liu** [2]

[1]Institute of Geology, Mineralogy and Geophysics, Ruhr University Bochum, Bochum, Germany, [2]Department of Earth and Planetary Sciences, McGill University, Montréal, Québec, Canada

Author contributions: *Conceptualization* M.P. Roth, A. Verdecchia. *Software* M.P. Roth. *Formal Analysis* M.P. Roth, A. Verdecchia. *Writing - original draft* M.P. Roth, A. Verdecchia. *Writing - Review & Editing* R.M. Harrington, Y. Liu. *Visualization* M.P. Roth, A. Verdecchia. *Funding acquisition* R.M. Harrington, Y. Liu.

Abstract Fluid injection/extraction activity related to hydraulic fracturing can induce earthquakes. Common mechanisms attributed to induced earthquakes include elevated pore pressure, poroelastic stress change, and fault loading through aseismic slip. However, their relative influence is still an open question. Estimating subsurface rock properties, such as pore pressure distribution, crack density, and fracture geometry can help quantify the causal relationship between fluid-rock interaction and fault activation. Inferring rock properties by means of indirect measurement may be a viable strategy to help identify weak structures susceptible to failure in regions where increased seismicity correlates with industrial activity, such as the Western Canada Sedimentary Basin. Here we present *in situ* estimates of V_p/V_s for 34 induced earthquake clusters in the Kiskatinaw area in northeast British Columbia. We estimate significant changes of up to $\pm$4.5% for nine clusters generally associated with areas of high injection volume. Predominantly small spatiotemporal V_p/V_s variations suggest pore pressure increase plays a secondary role in initiating earthquakes. In contrast, computational rock mechanical models that invoke a decreasing fracture aspect ratio and increasing fluid content in a fluid-saturated porous medium that are consistent with the treatment pressure history better explain the observations.

Production Editor: Gareth Funning
Handling Editor: Atalay Ayele Wondem
Copy & Layout Editor: Anant Hariharan

Received: March 16th, 2023
Accepted: September 13th, 2023
Published: November 15th, 2023

Non-technical summary The number of hydraulic-fracturing-induced earthquakes in Western Canada has risen significantly in the last two decades. Common mechanisms used to explain induced earthquakes include pore-pressure changes, stress changes in the rocks into which fluids are injected/extracted, and loading from slowly creeping faults near injection sites. One way to help identify causes of human-induced earthquakes is to measure changes in rock properties near injection wells, such as pressure increases, crack density, and crack shape. Here, we estimate such properties and their spatiotemporal changes by proxy using earthquake-wave velocity ratios. In combination with rock-mechanical models, we interpret mechanisms for changes in fault strength that can lead to earthquakes. Our results show predominantly small spatiotemporal variations in a total of 34 induced earthquake clusters that are inconsistent with the broad pore-pressure changes that are commonly used to explain induced earthquakes. We perform rock-mechanical modeling that provides a more consistent explanation for changes in rock properties. Our models suggest that the increasing fluid volume and increasingly narrow cracks in rocks near hydraulic fracturing treatment wells can alter rock strength in ways that are both consistent with rates and observed properties of earthquakes.

1 Introduction

Industrial subsurface operations that inject or extract fluid can activate fault slip that leads to felt seismicity. The triggering mechanisms most commonly invoked to explain induced fault activation include pore-pressure increases, poroelastic stress changes, and/or fault loading due to aseismic slip (e.g., Igonin et al., 2021; Schultz et al., 2020; Eyre et al., 2019). The relative importance of such mechanisms (and their relevant length scales) is still an open question that may be better answered with reliable estimates of subsurface rock mechanical properties, such as crack density and fluid-pressure distribution. For example, accelerated fluid diffusion driven by pore-pressure gradients resulting from sudden changes in porosity and permeability usually occur over relatively small length scales (Yu et al., 2019; Goebel and Brodsky, 2018). In contrast, elastic stress changes can surpass pressure perturbations at larger distances (e.g., Goebel et al., 2017; Keranen and Weingarten, 2018) where fluid flow plays a secondary role. Similarly, aseismic slip, i.e., creep along a stable fault segment, can outpace the pore pressure diffusion front and initiate rupture at an unstable fault segment (Bhattacharya and Viesca, 2019).

Sites where fluid injection correlates with induced earthquakes present unique opportunities to study fault

*Corresponding author: marco.roth@rub.de

activation processes under the influence of fluid-rock interaction. For example, high-volume, low-pressure wastewater disposal targeting a shallow reservoir at ∼1.3 km in southern Kansas induces earthquakes in basement layers at depths of 2-6 km. Some work suggests the combination of pore-pressure increase along permeable, basement-rooted faults and earthquake-earthquake interaction driven by coseismic static stress changes to be the leading mechanism for fault (re)activation (Cochran et al., 2018; Peterie et al., 2018; Verdecchia et al., 2021). In Oklahoma, Goebel et al. (2017) observed that pore-pressure increases and poroelastic stress changes played dominant roles in inducing earthquakes both proximal and distal to wells, respectively. In contrast, injection at hydraulic fracturing (HF) sites employs low fluid volume and high pressure relative to wastewater disposal in order to enhance hydraulic diffusivity in low-permeability reservoirs. Despite lower relative injection volume, the major oil and gas-bearing formations in the Western Canada Sedimentary Basin (WCSB) in northeast British Columbia and western Alberta commonly experience small (M<3) to occasionally moderate-sized (M∼4.5) injection-induced earthquakes (Atkinson et al., 2016). For example, the Kiskatinaw area (covering part of the Montney Formation) is one of the largest unconventional shale gas plays within the WCSB. Here, HF stimulation of the target formation at ∼2 km depth has induced several M 4+ earthquakes, including a M_w 4.6 on 17 August 2015 near Fort St. John (Babaie Mahani et al., 2017; Wang et al., 2020, 2021), a M_w 4.2 (M_L 4.5) on 30 November 2018 in the Kiskatinaw area (Babaie Mahani et al., 2019; Peña Castro et al., 2020), and a M_L 4.2 on 12 November 2022 near Fort St. John (Natural Resources Canada, 2023). The large distances over which comparatively small fluid-injection volumes induced M > 4 earthquakes on short time scales are puzzling. The low permeability of stimulated rock units implies that elevated pore pressure brought on by fluid diffusion is not the main stress-perturbation mechanism to activate faults. Recent modeling and observational work suggests that aseismic slip may also play a role in inducing some of the M 4+ events in the region (Guglielmi et al., 2015; Eyre et al., 2019; Yu et al., 2021). One fundamental step to identifying plausible mechanisms that are most consistent with observations of earthquake occurrence is through detailed studies of rock properties.

Lithology and rock physical properties can help delineate where pore pressure may be elevated, where fluid diffusivity properties may vary, and where rock strength may favor aseismic vs. seismic slip conditions. Specifically, lithology, crack density, fluid content, and/or fluid pressure, can induce measurable changes in rock properties, such as the compressional and shear wave velocities, V_p and V_s. Imaging the compressional-to-shear-wave velocity ratio, V_p/V_s, is therefore a meaningful tool for analyzing and interpreting fluid-related rock properties. In particular, several authors used V_p/V_s to infer changes in Poisson's ratio to detect the presence of fluid-filled cracks and quantify their properties (e.g., Zhao et al., 1996; Chevrot and van der Hilst, 2000; Takei, 2002). Other examples connect fluids in a rock volume to the weakness of the rock material. For instance, Yu et al. (2020) see a correlation between seismic attenuation and static stress drop for earthquakes at variable distances from the injection well. The authors conclude that higher seismic attenuation and a lower static stress-drop values proximal to injection sites result from higher fracture density and/or elevated pore pressure in the rock matrix (Worthington and Hudson, 2000) due to hydraulic stimulation. Similarly, Pimienta et al. (2018) observe anomalous V_p/V_s in subduction zones, which they interpret to result from zones of intense fracturing with high permeability ($> 10^{-16}$ m^2) and pore pressure.

In this study, we use seismological observations of HF-induced earthquakes to estimate the *in situ* V_p/V_s and use it as a proxy measurement of lithological properties and their relation to fluid injection. The term *in situ* in this context describes the localized damaged rock volume in which closely related earthquake pairs occur that are used to resolve V_p/V_s based on P- and S-arrival-time-differences within the pairs. The method was developed by Lin and Shearer (2007) and has been applied in various settings to document the spatiotemporal variation of V_p/V_s ratios within earthquake clusters, including sites with natural (Liu et al., 2023; Mesimeri et al., 2022; Lin and Shearer, 2021; Hsu et al., 2020) and induced seismicity (Lin, 2020). This work specifically aims to quantify the relative importance of rock damage and fluid pressure related to induced seismicity. To do so, we use continuous seismic records of 49 HF induced earthquake clusters in the Kiskatinaw area, British Columbia, Canada, between July 2017 and December 2020 to estimate *in situ* V_p/V_s ratios. We employ a method that compares differential travel times of co-located earthquakes to recover the V_p/V_s ratio of the source rock volume. We then compare our *in situ* estimates to grid values of a 3D velocity model for the complete time period in the study area. We show significant spatiotemporal variations of the *in situ* V_p/V_s ratio with respect to the underlying background model and discuss the reasons why the predominantly small spatiotemporal variations of V_p/V_s ratio do not point to a broad fluid-pressure increase. Namely, the lack of a broad change implies that pore-pressure increase is unlikely the leading triggering mechanism. Further, we compute the V_p/V_s ratio of an effective medium with varying crack aspect ratio and fluid volume content to infer the potential implications of fracture growth on rock strength. We show that the fracture/fluid evolution can explain the observed changes in V_p/V_s ratio and suggest an inverse correlation between seismicity rates and rock strength. The relative importance of aseismic vs. poroelastic triggering remains an open question due to a lack of direct evidence of aseismic slip.

2 Earthquake clusters and background velocity model

We use 8,731 earthquakes associated with HF operations in the Kiskatinaw area in the time period from 12 July 2017 to 31 December 2020 (updated from Roth et al.,

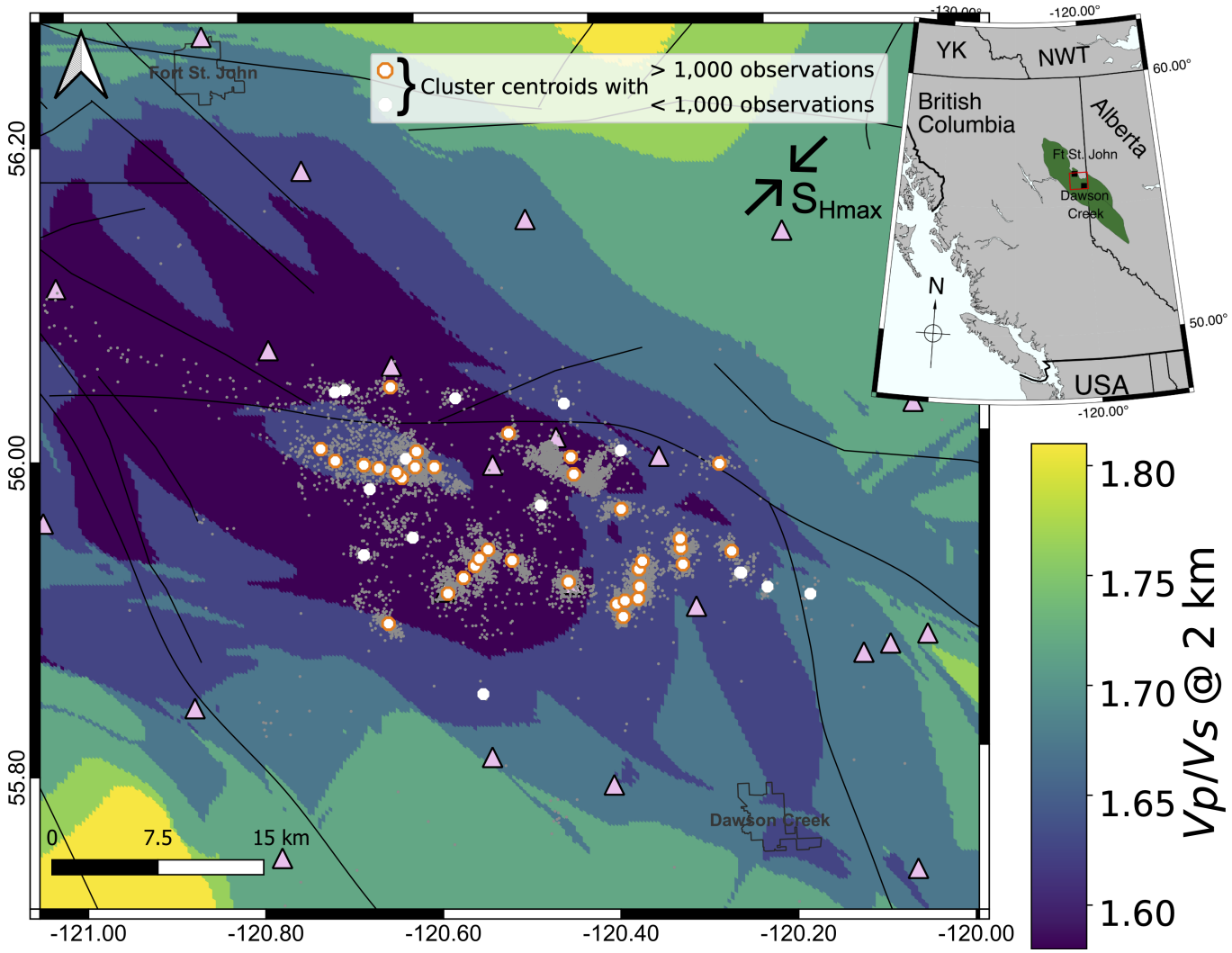

Figure 1 Overview of the Kiskatinaw area between Fort St. John (NW) and Dawson Creek (SE). Grey dots show 8,731 individual earthquake epicenters between 12 July 2017 to 31 December 2020. White dots show centroids of 49 spatiotemporally related earthquake clusters. Triangles denote seismic stations from networks XL, 1E, and PQ. Colorbar shows the starting model of V_p/V_s ratios at 2 km depth with mapped fault traces in black lines (Berger et al., 2009; Davies et al., 2018; Norgard, 1997). Estimates of regional S_{Hmax} are from Bell and Grasby (2012). Map inset shows the geographical extension of the Montney Formation (in green) and the Kiskatinaw area (red box). See Figure S1 for a detailed map of HF well locations and additional station information.

2020, Figure 1). The initial catalog results from an automated short-term average/long-term average (STA/LTA) trigger with analyst-reviewed phase arrivals. We refer to Roth et al. (2020) for details of the earthquake catalog development. The analysis here uses 25 broadband surface stations operated by McGill University, the Ruhr University Bochum, and Natural Resources Canada.

We define earthquake clusters in the group of 8,731 earthquakes analogous to Roth et al. (2020). First, we identify 32 time windows with at least four events on consecutive days. Second, we perform a waveform-similarity-based clustering approach within the time windows to identify spatial clustering. The two steps lead to classification of 49 event families, where each family is related to fluid injection in at least one HF well. Results from Roth et al. (2022) suggest that the clustered seismicity is related to the (re)activation of multiple optimally-oriented parallel left-lateral and strike-slip faults that are near the horizontal well trajectories of the respective HF wells. Unclustered seismicity exists as well, and is likely characterized by reverse-faulting mechanisms on deeper, isolated, and re-activated normal faults that were formed during the genesis of the Fort St. John graben system. The clustered events analysed here are therefore assumed to be associated with strike-slip faulting.

The method we use to estimate *in situ* V_p/V_s (described below) requires clustered seismicity. We describe changes of V_p/V_s using a reference 3D-velocity model calculated by Nanometrics Inc. The reference model is based on more than 100 compressional and 40 shear sonic logs, guided by 6 horizon top surfaces (Nanometrics Inc., 2020). The reference velocity model results from an optimization using a Particle Swarm Optimization method in an effort to obtain a smooth 3D model with an objective function weighted by phase residuals and event depth accuracy. It consists of estimates for V_p and V_s from which we calculate the V_p/V_s

ratios by element-wise division. As no error was reported for individual grid points, we apply a Gaussian error propagation with the assumption of 1.5% error per grid point (Supporting Information S1) and estimate an error of 2.12%, which is necessary for the high-resolution interpretation of the results. We note that the assumed uncertainty of 2.12% solely reflects the model error. The 140 sonic logs used to build the publicly available Nanometrics regional model do not enable resolving the velocity structure in high resolution or the geological structural complexity in the region.

3 Localized V_p/V_s estimation

The temporal and spatial proximity of individual earthquake clusters near wellbores (Figures 1, S1) allows focusing on the small rock volume affected by individual HF stimulation treatments. We adopt a method that compares the differential travel time differences of multiple inter-cluster earthquakes to recover the V_p/V_s ratio of the rock volume surrounding each cluster. We apply the method of Lin and Shearer (2007) that makes use of stationwise differential travel times between co-located event pairs with coincident ray paths, and removes the need to consider event origin times.

The method works by first considering that the differential S-wave travel time δt_s^i of an event pair is linearly related to the differential P-wave travel time δt_p^i per common station i by

$$\delta t_s^i = \left(\frac{V_p}{V_s}\right) \delta t_p^i + \delta t_0 \left(1 - \frac{V_p}{V_s}\right), \tag{1}$$

with δt_0 being the difference in origin times of the respective events. As the (4D-)origin information contains the sum of all errors, such as picking error, velocity-model uncertainty, and spatial errors, a cluster-wide, high-resolution method requires eliminating the absolute reference to temporal origin time information. To do so, Lin and Shearer (2007) establish a normalized version of Equation 1 by first calculating the mean values of the differential S- and P-times over all stations and then subtracting the normalized equation from Equation 1. The resulting equation relates the demeaned differential S-travel time ($\hat{\delta} t_s^i$) linearly to the P-travel times ($\hat{\delta} t_p^i$), by the coefficient V_p/V_s:

$$\hat{\delta} t_s^i = \left(\frac{V_p}{V_s}\right) \hat{\delta} t_p^i. \tag{2}$$

The V_p/V_s ratio as fitted in Equation 2 can be treated as a constant for each earthquake cluster, as long as the source-station distances are large compared to the hypocentral offsets among events in each cluster.

In addition, the P- and S-ray paths are assumed to have the same takeoff angles. As a final check on the suitability of the common ray-path assumption to the data set considered here, we compare the theoretical takeoff angles of direct P- and S-waves using TauP (Crotwell et al., 1999). We consider two sets of takeoff angles: (1) P- and S-angles for an individual event and (2) angles measured at hypothetical source-station distances of $<$5 km and $>$50 km for inter-event distances of 100 m. The hypothetical source-station distances reflect the observed range of source-station distances in our study area (Figure S2). We calculate arrivals using the IASP91 velocity model (Kennett and Engdahl, 1991). While P- and S-wave takeoff angles for shallow events ($<$2 km depth) at source-station distances of 5 to 50 km are approximately equal, the calculations show minor differences in takeoff angles on the order of $0.4°$ at source-station distances up to 5 km and inter-event distances of 100 m.

Liu et al. (2023) point out the importance of quality control criteria, which can have a major impact on the final V_p/V_s estimates. Our quality control procedure contains the following steps. We start with predefined event clusters based on waveform similarity detailed in Roth et al. (2020). We first identify time windows of consecutive days with a minimum of four events per day, and perform waveform-similarity clustering in each time window based on individual cross-correlation coefficients. Clusters are based on overall minimum correlation coefficients ranging from threshold values $\geq$ 0.6 up to 0.875. Next, we inspect the individual events in the defined clusters to remove potentially imprecise phase picks, i.e. erroneous phase arrivals, which result in perturbations to travel time curves. We do so by removing individual picks that deviate by more than 0.8 s or 2.5 s from predicted P- and S-wave arrival times based on constant velocities of 5.1 km/s and 2.9 km/s (comparable to the slope of the travel time curves in Figure S2), respectively. We note that the generally higher S-phase energy results in a more frequent cross-correlation correction of S-picks compared to P-phases, which have a lower signal-to-noise ratio. We then apply a cross-correlation-based picking correction to ensure that time-difference estimates come from exactly the same (relative) phase. We then further limit the calculation to stations with cross-correlation coefficients $>$ 0.8 for a given event pair to ensure the quality of the differential travel-time estimates, as even small deviations of the travel times from a linear travel time curve can lead to strong outliers (up to $\pm$0.15 s; Figure S2).

In the last steps of the quality-control procedure, we apply a hybrid L_1-L_2 fitting method (Huber, 1973, Figure S3) to automatically remove differential travel-time outliers that potentially bias numerical fitting. Initial analysis showed ambiguous V_p/V_s-ratio fits in the first analysis step for data sets with $<$ 300 observations (i.e., $\hat{\delta} t_s^i$ and $\hat{\delta} t_p^i$ observations per station among all event pairs). We therefore remove clusters with fewer than 300 observations to ensure robust fitting. The subsequent analysis step also initially showed uncertainties related to the number of observations. For example, clusters with $<$ 1,000 observations led to the lowest and highest estimates for V_p/V_s (Figure S4a) and the largest errors (Figure S4b). As a result, the relative difference between *in situ* estimates and the background model was initially largest for clusters with $<$ 1,000 observations (Figure S4c), suggesting a threshold of 1000 is required for robust observations. We therefore focus on clusters with $>$ 1,000 observations to eliminate any clear correlation between estimated V_p/V_s and the standard deviation of

the fit (Figure S4d). Finally, we perform a least-squares minimization linear curve fitting with the remaining dataset with a fixed y-intercept of 0 and a range for the slope varying between 0.8 and 5 for conservative and flexible fitting limits. Figure 2 shows a representative example of the linear regression in $\hat{\delta}t_s$ vs. $\hat{\delta}t_p$ differential body wave travel time differences.

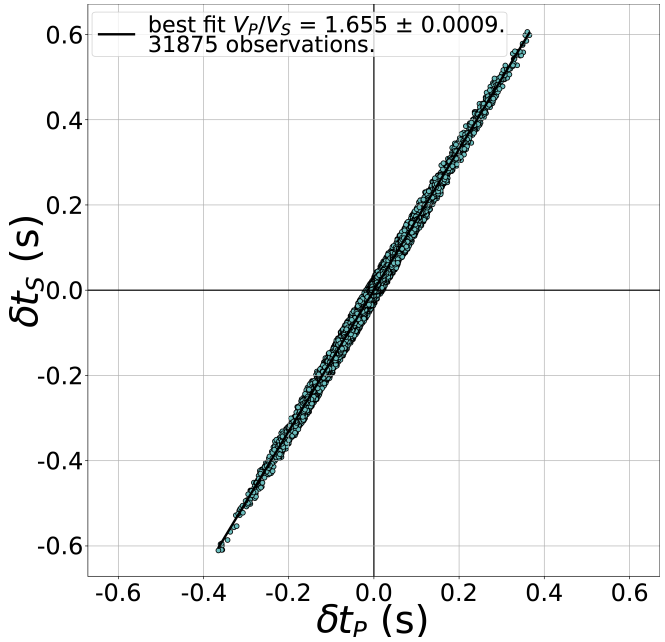

Figure 2 Representative example of a V_p/V_s ratio regression (black line) for one earthquake cluster. Each circle denotes the demeaned δt_s vs. δt_p differential travel time difference of one event pair recorded at a common station. The slope of the best-fit line returns the V_p/V_s estimate of the rock volume hosting the cluster as indicated in Equation 2.

4 V_p/V_s ratios of earthquake clusters

We estimate V_p/V_s ranging between 1.562 ± 0.0070 and 1.692 ± 0.0019 for a total of 34 clusters. The relative deviation of the *in situ* estimates with respect to the 3D background model varies between $\pm$4.5%. The two sections that follow first present the broad variation of V_p/V_s with respect to its spatiotemporal evolution and injected fluid volume (Figure 3) and then examine the evolution in more detail at an individual wellhead.

4.1 Broad spatiotemporal variations

Figure 3a shows the spatial variation of V_p/V_s changes normalized to the background value together with spatial variation of the injection volume (greyscale hexagons). Green and purple shaded dots show clusters with estimated increases and decreases of V_p/V_s relative to the background model, respectively. Figure 3b shows the relative variation of V_p/V_s along the NW-SE profile shown by the red dashed line in (a), as well as the time evolution in panel Figure 3(c) of the clusters. The dark, thicker vs. light, thinner green and purple shaded lines differentiate between significant and insignificant changes in V_p/V_s, respectively. (In other words, significance refers to a greater or less than 2.12% change from background and the linear regression, respectively; See Supporting Information S1 for further details). Out of the 34 clusters that pass the quality control criteria, 9 experience a significant V_p/V_s change, where 7 experience an increase, and 2 a decrease. The grey-shaded hexagons summarize the total injected fluid volume per HF wellhead within each hexagon in the time period from March 2013 to December 2020. We note that the injection history is reported from 2013 onward and the earthquake catalog starts in 2017. Figure 3a highlights four hexagons with injected fluid volume $>$ 1,000,000 m^3 that contain several cluster centroids (outlined in orange). It is noteworthy that all the highlighted areas experience a relative increase in V_p/V_s.

Figure 3 also shows 9 clusters with a relative V_p/V_s ratio change ranging between -1% and 1%, which we interpret as minor changes, despite their relative lower significance. We observe a moderate increase in V_p/V_s following fluid injection for 19 out of 34 clusters, and a moderate relative decrease for the remaining 6 clusters. The spatial distribution of estimates reveals a V_p/V_s ratio decrease that is concentrated primarily in the southeast part of the study area (Figure 3a-b).

The temporal evolution shown in Figure 3c suggests that the V_p/V_s ratio decreased relative to the starting model prior to ~May 2018 and was followed by a subsequent increase. However, we note that both the injection database and earthquake catalog do not cover the complete HF history of the study area. In addition, we do not see any change in V_p/V_s prior to and following the COVID-19 pandemic operational shutdown (Salvage and Eaton, 2021). As an independent check, we also use ambient seismic noise monitoring over the catalog time period to estimate background changes in the medium velocity (Lecocq et al., 2014). Figure S5 shows a change in $\delta v/v$ on the order of ± 0.05 % without clear temporal anomalies, consistent with an absence of significant V_p/V_s changes relative to the background model over time.

4.2 Variations at an individual wellhead

Earthquakes in the dataset generally follow a temporal migration in the direction of hydraulic fracturing stimulation (e.g. Roth et al., 2020). Seismicity typically begins in clusters near the end of a horizontal well (toe) and progressively migrates toward the vertical bending point (heel) of the horizontal well as stimulation proceeds. We examine the spatial migration pattern in further detail for a seismically active well with $>$ 100,000 observations (i.e., $\hat{\delta}t_s^i$ and $\hat{\delta}t_p^i$ estimates among all event pairs and stations) that occur between 12 March 2020 and 29 March 2020. We begin by first examining the two groups of wells with trajectories to the northwest and southeast of the wellhead, respectively. Figure 4 shows seven horizontal wells targeting the same shale layer at a depth of roughly 2.2 km. The high-resolution double-difference earthquake relocations show distinct clusters of seismicity centered around the three horizontal wells with southeastward trajectories (cyan box) and four horizontal wells with northwest trajectories (maroon box). Both clusters follow the timing of the stage

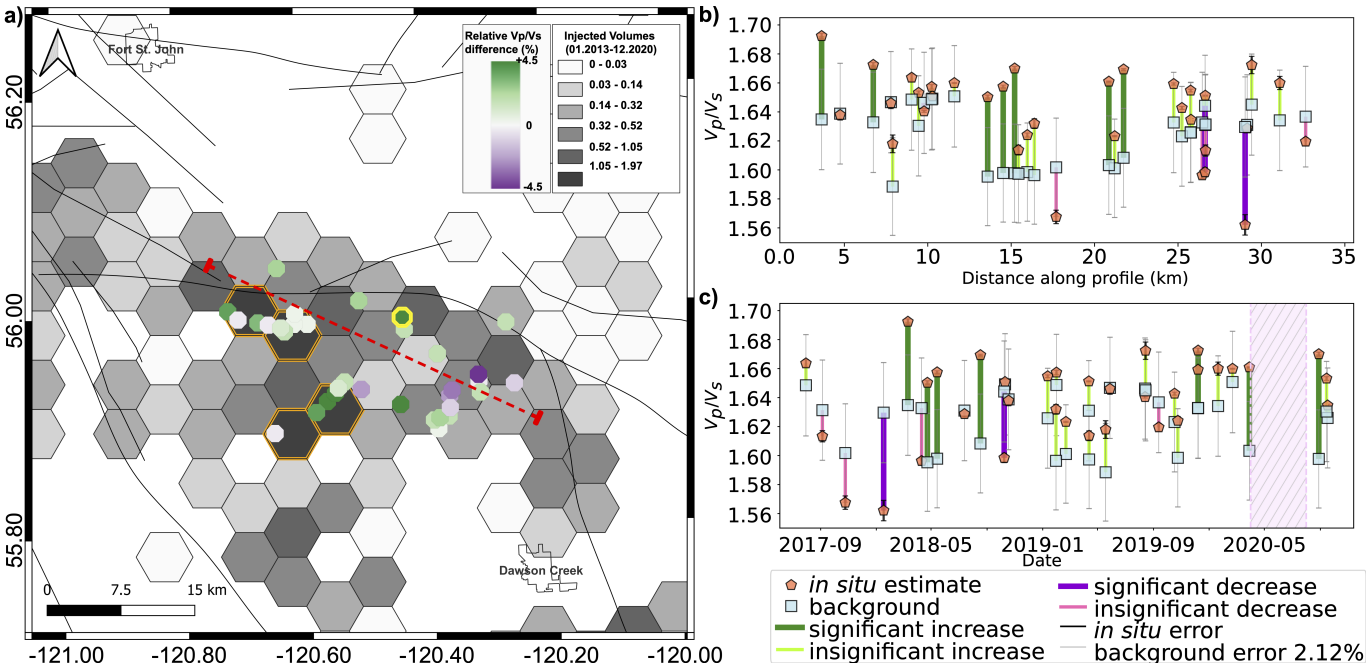

Figure 3 a) *In situ* V_p/V_s estimates per earthquake cluster relative to the reference model as in Figure 1. Green and purple show relative increases and decreases in V_p/V_s ratio relative to the background model, respectively. Greyscale shading is proportional to the total injection volume per HF wellhead within each hexagon from March 2013 to December 2020. The red line shows a profile along all clusters. The example cluster highlighted in yellow is further detailed in Figure 4. b) V_p/V_s estimates along the profile in a) from northwest (0 km) to southeast (37.07 km). Orange pentagons are *in situ* V_p/V_s estimates relative to the change in background value indicated by the light blue boxes. Green and purple shaded lines connecting the boxes highlight relative increases and decreases of V_p/V_s, respectively. Thick, dark lines describe significant changes that are larger than estimated errors and thin, light lines indicate changes that are within estimated errors. Black error bars are for the *in situ* V_p/V_s estimates, while grey error bars show the estimated 2.12% background model error (Section S1). c) Similar to b) but showing the temporal evolution during the catalog time period. The hatched, pink area shows the period of seismic quiescence due to suspension of HF operations (Salvage and Eaton, 2021) between April and August 2020.

stimulation. The southeast cluster exhibits a linear pattern that likely represents an activated structure that is several kilometers long. The northwest cluster (maroon box) contains multiple shorter, parallel lineations and a total of ~300 events.

We examine the northwest cluster (maroon box) in further detail by splitting the seismicity cluster into two subsets (Figure 4, red and blue tilted boxes). The choice of two subsets arises from a natural division between well-proximal (< 200 m from a hydraulic-fracturing stage; Figure 4 (blue box)) and well-distal (> 200 m; red box) events seen in the distribution of epicenters (Figure S7). There are 173 events in the 'proximal' subset (blue diagonal box), and 127 events in the 'distal' subset (red diagonal box). The individual V_p/V_s ratio regression fits for the two subsets are 1.648 ± 0.0009 (proximal) and 1.635 ± 0.0011 (distal).

We further examine the temporal variation within the northwestern seismicity cluster (Figure 4, larger maroon box). As the seismicity migration direction largely follows the direction of HF-stage stimulation and broadly follows the same timing, we divide the cluster into smaller subsets with similar timing. For example, Figure 5a-d shows the chronological division of 300 events in the northwestern cluster in Figure 4 (maroon box) into four equally sized groups of 67 to 68 events in non-overlapping windows. We note that applying quality control criteria removes certain event pairs and hence reduces the number of grouped events from the original 300 to 269. The temporal progression of estimated V_p/V_s values (Figure 5e) shows a slight initial decrease from the starting value of 1.653 (Figure 5a-b), followed by a steep decrease to a minimum of 1.590 (Figure 5c, corresponding to a total decrease of ~3.8%, comparable to the regional observed maximum of ± 4.5%). The V_p/V_s then rebounds to a comparable value of 1.631. The seemingly small absolute changes in V_p/V_s in the range of 0.06 are already significant with respect to reported values between 1.98 and 1.42 (Gregory, 1976), which were estimated for different types of consolidated sedimentary rocks with porosities ranging from 4.45% to 41.1%, water-air-saturation ratios ranging from 0% to 100%, and confining pressures ranging from 0 MPa to ~69 MPa. Figure S8 shows a consistent trend and similar V_p/V_s variation when testing variable event group sizes that range from three to six groups with 90 to 44 events per group, respectively. There are three additional clusters in the entire data set with > 100,000 observations (Table S1, Figure S9), which include the southeast cluster in Figure 4 (cyan box). They exhibit similar temporal evolution with a minimum V_p/V_s in the intermediate HF stages.

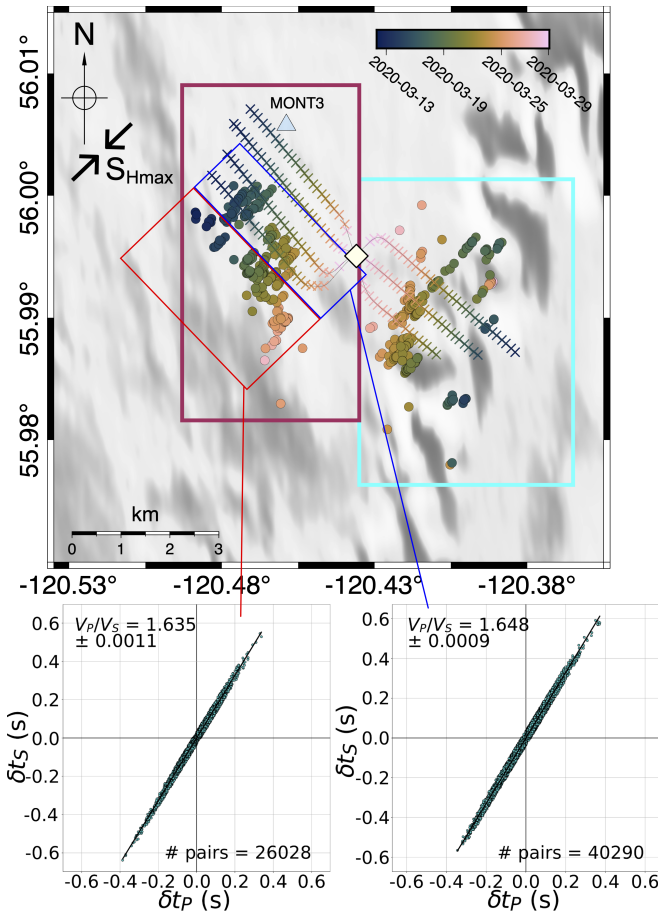

Figure 4 One example cluster from Figure 3a (outlined in yellow). High-resolution earthquake relocations show two distinct earthquake clusters near seven diametrically opposed well trajectories (lines) extending from a single wellhead (white diamond). Hatched lines on the well trajectories are individual HF injection stage locations with timing indicated by the colorbar. Earthquake epicenters (colored dots) have origin times marked by the same colorbar. The cyan and maroon boxes separate the southeastern and northwestern clusters, respectively. Blue and red boxes show subsets of the northwestern cluster described as HF-stage proximal (distance < 200 m) and distal (> 200 m), respectively (see text). The respective V_p/V_s ratio regression plots the two subsets shown below the map with each corresponding box color. Figure S6 shows the respective distribution of hypocentral depths.

5 Fracture evolution

In order to interpret the V_p/V_s estimates in the context of rock properties and fluid injection, we develop physical rock mechanics models to investigate the consistency with injection history. Specifically, we vary sets of material properties and elastic constants (e.g., bulk and shear modulus) in an effective medium to test their effects on the seismic wave velocities (related to an effective density) and the V_p/V_s ratio. An effective rock volume consists of a rock matrix and fluid-filled voids and cavities such as fractures and pores. Multiple physical properties, such as fluid fraction, elastic modulus of each medium component, and/or fracture geometry, control the elastic moduli of the effective porous medium. As the seismic body-wave velocities depend on the effective elastic moduli and rock densities, so will the V_p/V_s ratio. Hence, the increase or decrease of V_p/V_s will directly depend on fluid content and pore geometry (e.g., Takei, 2002; Brantut and David, 2019).

To explore the observed *in situ* V_p/V_s changes and their dependence on the rock matrix and resultant fluid content, we use a model with randomly oriented spheroidal, fully water-saturated pores. We model fluid content with porosity Φ and pore shape with the aspect ratio α, where $0 < \alpha \leq 1$. An aspect ratio of $\alpha = 1$ describes a sphere, where increasingly smaller values describe thin ellipsoids. We apply self-consistent estimates for bulk and shear moduli, K and μ, respectively, from Berryman (1980) to estimate V_p/V_s for an effective medium with aspect ratios ranging between $10^{-3} \leq \alpha \leq 1$ and fluid content ranging from $0 \leq \Phi \leq 0.2$. We use six iterations to numerically solve the self-consistent estimates (Figure S10). The model does not violate the (arithmetic) upper Voigt (Voigt, 1910) and lower Reuss boundaries (Reuss, 1929) and fulfills the Hashin-Shtrikman bounds (Hashin and Shtrikman, 1963) for isotropic, linear and elastic media for the most common geometries. We model the shale layers of the Montney Basin using $K = 35$ GPa and $\mu = 25$ GPa, which is in general agreement with global observations of shale reservoirs (Omovie and Castagna, 2020). We use $K = 2.2$ GPa and $\mu = 0$ GPa for the pore fluid and explore the model space of changes in V_p/V_s as a function of porosity and crack aspect ratio (see Figure S11).

We then combine the impact of both the aspect ratio and the fluid fraction (porosity) on the bulk and shear moduli (shown in Figure S11) into individually evolving trends to estimate the effective V_p/V_s based on the two moduli (Figure 6a). We allow the trends to vary in both aspect ratio and porosity in order to explore consistency scenarios with injection history and determine how the two free parameters might influence V_p/V_s evolution (Figure 6). The range of porosity/aspect ratio pairs can lead to highly varying V_p/V_s estimates. For illustration purposes, Figure 6a only displays values between 1.65 and 2.1 that cover the initial V_p/V_s values observed by Gregory (1976). Specifically, we explore four possible trajectories: (1) a large decrease in aspect ratio and a small increase in fluid content (Figure 6 orange lines, with $\log(\alpha)_{init} = -0.1$, $\log(\alpha)_{final} = -2.25$ and $\Phi_{init} = 0.01$, $\Phi_{final} = 0.02$), (2) a moderate decrease in aspect ratio and moderate increase in fluid content (Figure 6 beige lines, with $\log(\alpha)_{init} = -0.1$, $\log(\alpha)_{final} = -1.75$ and $\Phi_{init} = 0.01$, $\Phi_{final} = 0.05$), and (3) a small decrease in aspect ratio and large increase of fluid content (Figure 6 copper-colored lines, with $\log(\alpha)_{init} = -0.1$, $\log(\alpha)_{final} = -1.25$ and $\Phi_{init} = 0.01$, $\Phi_{final} = 0.15$), and (4) a segmented trajectory with an initial increase in fluid fraction and subsequent decrease in aspect ratio (Figure 6 red lines, with $\log(\alpha)_{init} = -0.1$, $\log(\alpha)_{final} = -1.15$ and $\Phi_{init} = 0.01$, $\Phi_{final} = 0.105$). Although the detailed geological well reports do not provide insights into the aspect ratio, the porosity of the Montney Formation is documented to be between 1% and 3%, where local differences of up to 5%+ can occur (BC-ER, 2023).

Figure 6a shows that V_p/V_s decreases slowly with de-

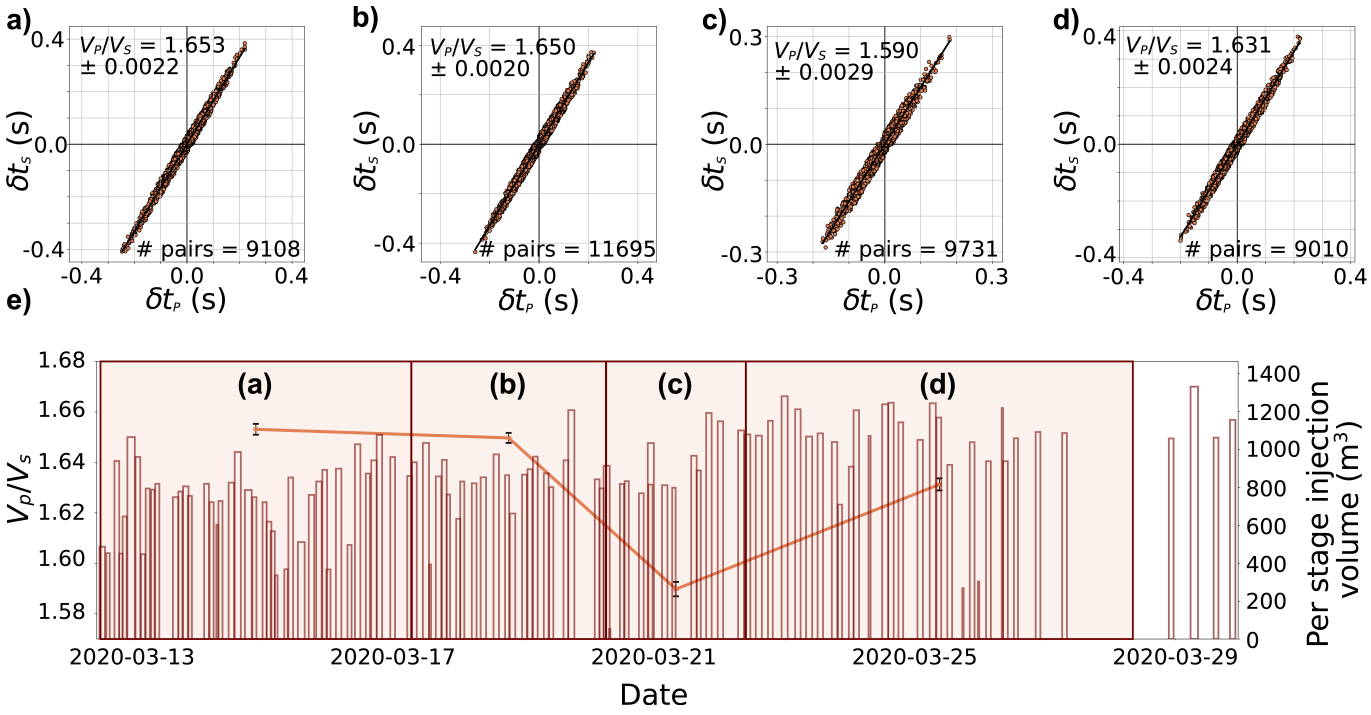

Figure 5 Temporal evolution of V_p/V_s ratios of the northwestern event cluster in Figure 4 (maroon box). a)-d) show equally-sized temporal groups of 67-68 events per group. e) shows the temporal V_p/V_s progression (orange line) along with the injected fluid volume per stage (red bars). Bright orange shading highlights the time period in which each successive temporal subset of earthquakes was active.

creasing aspect ratio and increasing porosity (fluid content) when aspect ratios are above values of α greater than $\sim$ 0.03-0.1 ($\log \alpha > -1.5$). The most significant V_p/V_s changes are exhibited at lower aspect ratios ($\alpha <\sim$ 0.03-0.1), where V_p/V_s increases rapidly with decreasing aspect ratio and moderately increases with porosity. It is logical to assume that during HF-stimulation, fluid content first increases before fracture growth is promoted. Once significant fracture growth initiates, the fracture aspect ratio decreases as crack geometry becomes thin and elongated. The interplay and relative timing of the porosity increase and aspect ratio changes during HF-stimulation likely correspond to scenario #4, where a significant increase in fluid volume and porosity occurs first, followed by a rapid decrease in aspect ratio. The trajectory #4 in 6 (maroon line) would therefore correspond to an initial drop of V_p/V_s in the early to intermediate HF stages, followed by subsequent increases in V_p/V_s towards the end of HF stimulation. Scenario #4 is also most consistent with the data (blue line). We note that Figure 6 is not intended to precisely model the fluid-fracture evolution, but rather as a consistency check. It shows that in the scenario which most likely emulates porosity and aspect ratios during HF-stimulation, both effects of (i) decreasing fracture aspect ratios and (ii) increases in fluid fraction can lead to an initial decrease followed by an increase in V_p/V_s. In reality, the relative amplitudes of V_p/V_s decrease and increase, hence the overall change before and after a HF treatment, will depend on the exact fluid-rock mechanical property trajectory. Therefore, it is possible to observe bulk V_p/V_s decreases following fluid injection activity. It is important to note that the rock physical model shown in Figure 6 accounts for two-phase porous media with approximated estimates of elastic moduli and only one pore geometry. Nevertheless, the two-phase model is still able to capture the same spatial-temporal trend in observations.

6 Discussion

The following sections first describe how pore pressure variation can explain the role of fluids in the observed V_p/V_s changes and then discuss the implications of V_p/V_s changes in the context of injection history for earthquake triggering mechanisms. We will then compare our results to effective-medium models and rock physics analysis as a consistency check on our interpretations.

6.1 The impact of fluids on V_p/V_s

Lin (2020) applies the *in situ* V_p/V_s estimate methodology (Lin and Shearer, 2007) to induced seismicity. To the best of our knowledge, this study is the first to apply the method to a HF-induced seismicity setting. Although both settings involve fluid-injection, we see remarkable differences in the study sites. Our results point to neither systematic operationally-related increases nor decreases of V_p/V_s. On the contrary, Gritto and Jarpe (2014) found a positive correlation between increasing V_p/V_s and total injected water volume at the Geysers geothermal field. They conclude that V_p/V_s estimates can be interpreted to predict fluid saturation changes around injection wells. They found that long-term fluid injection led to an observed V_p/V_s increase of $\sim$6%. Lin (2020) observes a decrease in V_p/V_s accompanying the

extraction of water at the Salton Sea geothermal field and subsequent increases in V_p/V_s as the reservoir replenishes. The long-term net fluid production at the Salton Sea geothermal field led to a decrease of up to ∼7%, which is consistent with the above interpretations (Lin, 2020). By comparison, the V_p/V_s changes associated with short-term HF operation observed here are within -4% and 4.5%. However, at geothermal power plants, the driving mechanism for changes in V_p and V_s would be pore pressure variation, fluid diffusion, and/or fluid saturation. Assuming a saturated medium at seismogenic depths, an increase in fluid volume would cause a relative increase in V_p and decrease in V_s (e.g. Han and Batzle, 2004), leading to an absolute increase in V_p/V_s. For example, Winkler and Nur (1982) showed in laboratory measurements that the V_p/V_s ratio of fully saturated rock samples is higher compared to V_p/V_s ratios of partially (∼90%) saturated or dry samples.

Another well-known mechanism to increase V_p/V_s is tensile fracture opening. Brantut and David (2019) describe that in a fully fluid-saturated setting, a fracture opening is equivalent to the reduction of confining pressure. Experimental data confirm an increase of V_p/V_s with decreasing confining pressure that occurs as the pore pressure inside fluid-filled cracks increases (Christensen, 1984). The scenario is in agreement with observations of Dawson et al. (1999) and McNutt (2005), who interpreted seismic tomographic images of high V_p/V_s zones at the Kilauea Caldera, Hawaii, to be either highly fractured material or the accumulation of partial melt. Similar to HF operations in this study, fracturing below the volcano might result from volumetric changes (tensile opening) while melt ascends (Schmid et al., 2022). Seismic events resulting from tensile fracture opening as a direct result of HF operations are most likely associated with microseismicity (M_w < 0; Eaton et al., 2014; Bohnhoff et al., 2009) aligned perpendicular to the direction of the minimum horizontal regional stress. The detailed relocations and fault plane solutions (where available) of seismicity in our study area suggest that the earthquakes with typical magnitudes of M_L > 0 occur primarily on (likely) reactivated, optimally-oriented strike-slip faults (Roth et al., 2020, 2022). Neither fluid saturation nor changes in confining pressure and/or fracture model fully describe the observed V_p/V_s ratio changes in the observations presented here.

Our results do not represent trends that have been observed from geothermal systems and/or fracture opening scenarios. Hence, we have to invoke more complex mechanisms and models that explain how HF operations can affect V_p/V_s. For example, Gosselin et al. (2020) and Wang et al. (2022) interpret V_p/V_s changes at the northern Cascadia and Hikurangi margins, respectively, with phases of fluid-pressure increase and dissipation caused by fault-valve behavior. HF treatments in Kiskatinaw in a fully fluid-saturated rock initiate tensile fracture growth near the stages that correspond to decreasing fracture aspect ratios and increasing fluid content. We explore various physical models of fluid-saturated rocks to infer how fracture growth affects rock strength. One fundamental assumption is that HF treatments (re)activate faults and modify the existing fractures (in addition to creating new ones). Figures 6a and S10 show our theoretical estimates of V_p/V_s for an effective fluid-saturated porous two-phase medium (a rock matrix and pore fluid) leading to variable V_p/V_s values when allowing the aspect ratio and fluid-saturated porosity to vary.

Figure S11 shows a relatively rapid decrease in shear modulus with increasing fluid content when aspect ratios are small. The shear modulus decrease leads to a decreased shear wave velocity V_s, (which is dependent on the shear modulus and effective porosity), and a corresponding slower decrease in V_p. Hence, V_p/V_s could potentially exceed the suggested limits by Gregory (1976) for small aspect ratios and high fluid content. Figure S12 illustrates the impact of small aspect ratios, where large aspect ratios ($0.1 \leq \alpha \leq 1$; i.e. spheroid to penny-shaped fractures) lead first to a decrease V_p/V_s with increasing fluid content. Conversely, small aspect ratios ($0.001 < \alpha < 0.03$) lead to rapid increase in V_p/V_s.

One limiting factor of our work is in the reference velocity model. While Nanometrics Inc. (2020) utilized all available data at the time to develop the velocity model, it is likely a small fraction of a more comprehensive dataset required to resolve the geological complexity of the study area. Due to the existing resolution limit of the reference velocity model, we can not rule out that larger changes in V_p/V_s (and hence velocity changes) are due to reference model uncertainties rather than only due to realistic changes in the earthquake cluster areas.

6.2 Earthquake triggering mechanisms

The *in situ* V_p/V_s estimates in this study result from seismological observations. As such, the results presented here are implicitly limited in space and time to the rock volume affected by fault (re)activation, as well as the starting 3D velocity model (Figure 1). To avoid over-interpretation of V_p/V_s changes, we consider estimates outside of the assumed 2.12% error in the reference 3D velocity model (Section S1) in addition to the standard deviation inferred from the linear regression (Figure 2) to be significant. With respect to the aforementioned error and uncertainty estimates, 25 out of 34 V_p/V_s estimates do not deviate significantly from the underlying background model, and therefore do not imply any significant V_p/V_s variation resulting from fluid injection. Nine out of 34 V_p/V_s estimates show significant increases or decreases relative to background values. The areas within the hexagons in Figure 3 with high cumulative injection volume (outlined in orange) would experience large anticipated increases in pore pressure, similar to increases observed at geothermal sites (Gritto and Jarpe, 2014). Large pore pressure increases that result as a consequence of fluid injection would cause a reduction of effective stresses, and would be consistent with earthquake triggering in a classical Mohr-Coloumb-failure framework. On the other hand, we also observe significant V_p/V_s decreases in areas with large amounts of injected fluid (southeast end of the profile in Figure 3), suggesting that additional factors to pore pressure increase may have an important

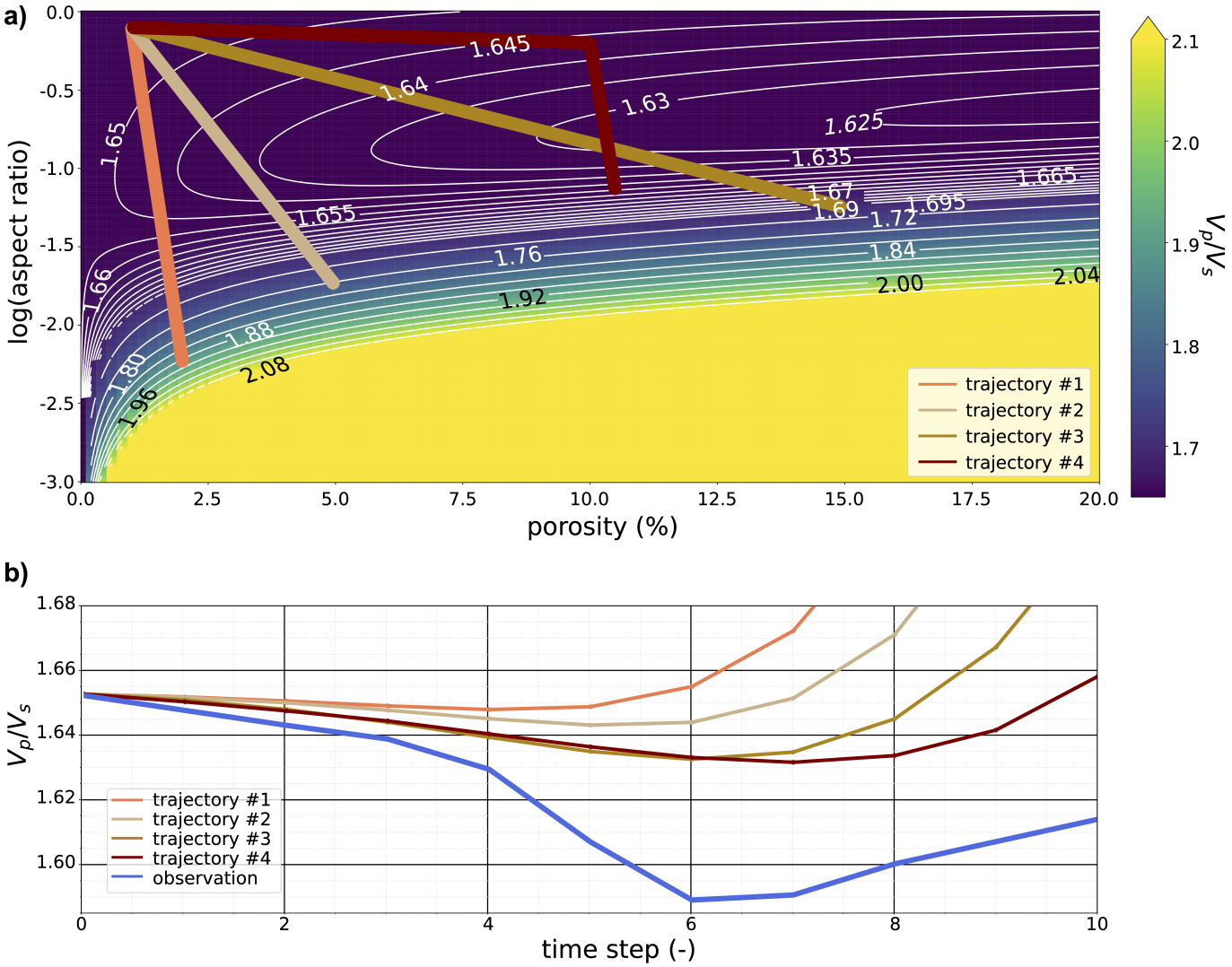

Figure 6 a) Theoretical V_p/V_s ratio (colorbar) as a function of crack aspect ratio and fraction of fluids in the effective medium (porosity). The four trajectories show scenarios of possible fracture and fluid evolution with V_p/V_s computed according to the self-consistent estimates in Berryman (1980). b) Conceptual V_p/V_s ratio per fracture evolution in a), as a function of HF operation time. The line colors of the four scenarios correspond to the colors in (a), and the blue curve shows the estimated mean *in situ* V_p/V_s with interpolated time progression as from Figures 5 and S8.

role in activating faults here. In other words, the lack of large-scale V_p/V_s increase expected from fluid injection and corresponding pore pressure increase suggests broad significant fluid-pressure increases are not sufficient to explain the induced seismicity in Kiskatinaw, at least on their own.

Poroelastic stress changes and fault loading from aseismic slip can (re)activate faults and general zones of weakness over a large range of distances compared to pore pressure changes (e.g., Deng et al., 2016; Bhattacharya and Viesca, 2019). In addition, tensile fracture opening adjacent to HF stages in the target formation can result in static elastic stress transfer that can trigger seismicity in close proximity (Kettlety et al., 2020). The rock volume that hosts seismicity need not experience significant V_p/V_s changes. Other studies have observed direct or indirect evidence of slow and aseismic slip in western Canada (e.g., Eyre et al., 2022; Yu et al., 2021). However, the observations in this study do not indicate any correlation of the earthquake clusters to aseismic slip. Therefore, we are unable to definitively capture the relative importance between poroelastic and aseismic slip triggering in the study area based on V_p/V_s changes inferred from seismological observations alone. Nevertheless, the results presented here suggest rock properties play an equally important role in fault activation as pore pressure changes.

7 Conclusion

We present *in situ* estimates of V_p/V_s ratios based on spatiotemporally correlated clusters of HF-induced earthquakes in the Kiskatinaw area in the Montney Formation, British Columbia, between July 2017 and December 2020. Out of the 49 clusters analyzed, 34 contain $>$ 1,000 body wave differential travel-time observations that enable robust fitting with no clear correlation between estimated V_p/V_s and the standard deviation of the fit. Among the 34 clusters, 9 indicate significant changes of up to $\pm$ 4.5%, beyond the error range of 2.12% of the starting velocity model. The spatiotemporal heterogeneity in V_p/V_s suggests broad pore-pressure

increases are not singularly sufficient to explain the induced earthquakes. Considering the V_p/V_s variations in the context of rock physical models and injection history suggests that rock physical properties may have an equally influential role in triggering. The absence of clear evidence for aseismic slip leaves the question open regarding the relative importance of aseismic slip vs. poroelastic triggering.

Exploring various compositions of fluid-saturated porous media shows the evolution of fracture growth and changing fluid content can explain the observed changes in V_p/V_s ratios. It also suggests that seismicity rates may inversely correlate with changing rock strength conditions. The observed V_p/V_s ratios first decrease with increasing fluid content, followed by increases at intermediate HF stages, presumably coincident with fracture growth, i.e., when aspect ratio decreases. The model's consistency with the observations demonstrates the utility of effective media in interpreting the role of rock properties in controlling fault activation, in concert with seismic observations.

Acknowledgements

This project is partially funded by the Deutsche Forschungsgemeinschaft (DFG, German Research Foundation)—Project Number 428868223, Ruhr University Bochum (RUB) New Faculty startup funds, and Natural Sciences and Engineering Research Council of Canada (NSERC) Strategic Partnership Grant for Projects 494141-2016. The authors would like to acknowledge H. Kao from Natural Resources Canada (NRCan), G. Langston, J. Onwuemeka, B. Wang, and C. Esteve (at McGill University, and NRCan during the time of this study), for help in seismic station deployment and maintenance. The authors would also like to thank S. Venables, M. Gaucher, and British Columbia Energy Regulator staff for providing well data, the 3D reference velocity model, and logistical support, and K. D. Fischer from RUB Seismological Observatory for help in data acquisition. We want to thank E. Korkolis (RUB) for discussions on rock mechanical work approaches and feedback for the manuscript. We thank Editor Atalay Ayele Wondem and two anonymous reviewers for their constructive comments that helped to improve the quality of this manuscript.

Data and code availability

Waveform data used in this study are archived at IRIS under network codes XL, 1E, and PQ (e.g., https://ds.iris.edu/gmap/XL). Well data are provided by British Columbia Energy Regulator (BC-ER; https://www.bc-er.ca/data-reports/data-centre/, last accessed August 2022). The seismicity catalog used in this study was maintained using SeisComP3 (Weber et al., 2007) and can be accessed via https://doi.org/10.5281/zenodo.5152857. Figures were made using Matplotlib v3.3.2 (Hunter, 2007), and maps were made with GIS v3.22.3 (QGIS Development Team, 2022) and Generic Mapping Tools v6.1.1 (Wessel et al., 2019). Topographic information comes from Jarvis et al. (2008). The reference 3D velocity model was provided by Nanometrics Inc. and BC-ER (Nanometrics Inc., 2020). We used the ObsPy toolbox v1.2.2 for seismological data processing Beyreuther et al. (2010). We use color maps from Crameri (2021).

Competing interests

The authors declare that they have no conflict of interest.

References

Atkinson, G. M., Eaton, D. W., Ghofrani, H., Walker, D., Cheadle, B., Schultz, R., Shcherbakov, R., Tiampo, K., Gu, J., Harrington, R. M., Liu, Y., van der Baan, M., and Kao, H. Hydraulic Fracturing and Seismicity in the Western Canada Sedimentary Basin. *Seismological Research Letters*, 87(3):631–647, 2016. doi: 10.1785/0220150263.

Babaie Mahani, A., Schultz, R., Kao, H., Walker, D., Johnson, J., and Salas, C. Fluid injection and seismic activity in the northern Montney play, British Columbia, Canada, with special reference to the 17 August 2015 Mw 4.6 induced earthquake. *Bulletin of the Seismological Society of America*, 107(2):542–552, 2017. doi: 10.1785/0120160175.

Babaie Mahani, A., Kao, H., Atkinson, G. M., Assatourians, K., Addo, K., and Liu, Y. Ground-Motion Characteristics of the 30 November 2018 Injection-Induced Earthquake Sequence in Northeast British Columbia, Canada. *Seismological Research Letters*, 90 (4):1457–1467, 2019. doi: 10.1785/0220190040.

BC-ER. Well Lookup and Reports, 2023. Data retrieved from BC-ER Data Centre, https://www.bc-er.ca/data-reports/data-centre/.

Bell, J. and Grasby, S. The stress regime of the Western Canadian Sedimentary Basin. *Geofluids*, 12(2):150–165, 2012. doi: 10.1111/j.1468-8123.2011.00349.x.

Berger, Z., Boast, M., and Mushayandebvu, M. The contribution of integrated HRAM studies to exploration and exploitation of unconventional plays in North America. *Canadian Society of Petroleum Geologists, Reservoir*, 36:40–45, 2009.

Berryman, J. G. Long-wavelength propagation in composite elastic media II. Ellipsoidal inclusions. *The Journal of the Acoustical Society of America*, 68(6):1820–1831, 1980. doi: 10.1121/1.385172.

Beyreuther, M., Barsch, R., Krischer, L., Megies, T., Behr, Y., and Wassermann, J. ObsPy: A Python Toolbox for Seismology. *Seismological Research Letters*, 81(3):530–533, 2010. doi: 10.1785/gssrl.81.3.530.

Bhattacharya, P. and Viesca, R. C. Fluid-induced aseismic fault slip outpaces pore-fluid migration. *Science*, 364(6439):464–468, 2019. doi: 10.1126/science.aaw7354.

Bohnhoff, M., Dresen, G., Ellsworth, W. L., and Ito, H. Passive Seismic Monitoring of Natural and Induced Earthquakes: Case Studies, Future Directions and Socio-Economic Relevance. In *New Frontiers in Integrated Solid Earth Sciences*, pages 261–285. Springer Netherlands, 2009. doi: 10.1007/978-90-481-2737-5_7.

Brantut, N. and David, E. C. Influence of fluids on V_p/V_s ratio: increase or decrease? *Geophysical Journal International*, 216(3): 2037–2043, 2019. doi: 10.1093/gji/ggy518.

Chevrot, S. and van der Hilst, R. D. The Poisson ratio of the Australian crust: geological and geophysical implications. *Earth and Planetary Science Letters*, 183(1-2):121–132, 2000. doi: 10.1016/s0012-821x(00)00264-8.

Christensen, N. I. Pore pressure and oceanic crustal seismic structure. *Geophysical Journal International*, 79(2):411–423, 1984. doi: 10.1111/j.1365-246x.1984.tb02232.x.

Cochran, E. S., Ross, Z. E., Harrington, R. M., Dougherty, S. L., and Rubinstein, J. L. Induced Earthquake Families Reveal Distinctive Evolutionary Patterns Near Disposal Wells. *Journal of Geophysical Research: Solid Earth*, 123(9):8045–8055, 2018. doi: 10.1029/2018jb016270.

Crameri, F. Scientific colour maps. *Zenodo*, 7.0.1, 2021. doi: 10.5281/zenodo.1243862.

Crotwell, H. P., Owens, T. J., and Ritsema, J. The TauP Toolkit: Flexible Seismic Travel-time and Ray-path Utilities. *Seismological Research Letters*, 70(2):154–160, 1999. doi: 10.1785/gssrl.70.2.154.

Davies, G. R., Watson, N., Moslow, T. F., and MacEachern, J. A. Regional subdivisions, sequences, correlations and facies relationships of the Lower Triassic Montney Formation, west-central Alberta to northeastern British Columbia, Canada — with emphasis on role of paleostructure. *Bulletin of Canadian Petroleum Geology*, 66(1):23–92, 2018.

Dawson, P. B., Chouet, B. A., Okubo, P. G., Villaseñor, A., and Benz, H. M. Three-dimensional velocity structure of the Kilauea Caldera, Hawaii. *Geophysical Research Letters*, 26(18): 2805–2808, 1999. doi: 10.1029/1999gl005379.

Deng, K., Liu, Y., and Harrington, R. M. Poroelastic stress triggering of the December 2013 Crooked Lake, Alberta, induced seismicity sequence. *Geophysical Research Letters*, 43(16):8482–8491, 2016. doi: 10.1002/2016gl070421.

Eaton, D. W., van der Baan, M., Birkelo, B., and Tary, J.-B. Scaling relations and spectral characteristics of tensile microseisms: evidence for opening/closing cracks during hydraulic fracturing. *Geophysical Journal International*, 196(3):1844–1857, 2014. doi: 10.1093/gji/ggt498.

Eyre, T. S., Eaton, D. W., Garagash, D. I., Zecevic, M., Venieri, M., Weir, R., and Lawton, D. C. The role of aseismic slip in hydraulic fracturing–induced seismicity. *Science Advances*, 5(8): eaav7172, 2019. doi: 10.1126/sciadv.aav7172.

Eyre, T. S., Samsonov, S., Feng, W., Kao, H., and Eaton, D. W. InSAR data reveal that the largest hydraulic fracturing-induced earthquake in Canada, to date, is a slow-slip event. *Scientific Reports*, 12(1), 2022. doi: 10.1038/s41598-022-06129-3.

Goebel, T., Weingarten, M., Chen, X., Haffener, J., and Brodsky, E. The 2016 Mw5.1 Fairview, Oklahoma earthquakes: Evidence for long-range poroelastic triggering at $>$40 km from fluid disposal wells. *Earth and Planetary Science Letters*, 472:50–61, 2017. doi: 10.1016/j.epsl.2017.05.011.

Goebel, T. H. W. and Brodsky, E. E. The spatial footprint of injection wells in a global compilation of induced earthquake sequences. *Science*, 361(6405):899–904, 2018. doi: 10.1126/science.aat5449.

Gosselin, J. M., Audet, P., Estève, C., McLellan, M., Mosher, S. G., and Schaeffer, A. J. Seismic evidence for megathrust fault-valve behavior during episodic tremor and slip. *Science Advances*, 6 (4), 2020. doi: 10.1126/sciadv.aay5174.

Gregory, A. R. Fluid saturation effects on dynamic elastic properties of sedimentary rocks. *GEOPHYSICS*, 41(5):895–921, 1976. doi: 10.1190/1.1440671.

Gritto, R. and Jarpe, S. P. Temporal variations of V_p/V_s-ratio at The Geysers geothermal field, USA. *Geothermics*, 52:112–119, 2014. doi: 10.1016/j.geothermics.2014.01.012.

Guglielmi, Y., Cappa, F., Avouac, J.-P., Henry, P., and Elsworth, D. Seismicity triggered by fluid injection–induced aseismic slip. *Science*, 348(6240):1224–1226, 2015. doi: 10.1126/science.aab0476.

Han, D. and Batzle, M. L. Gassmann's equation and fluid-saturation effects on seismic velocities. *GEOPHYSICS*, 69(2):398–405, mar 2004. doi: 10.1190/1.1707059.

Hashin, Z. and Shtrikman, S. A variational approach to the theory of the elastic behaviour of multiphase materials. *Journal of the Mechanics and Physics of Solids*, 11(2):127–140, 1963. doi: 10.1016/0022-5096(63)90060-7.

Hsu, Y.-F., Huang, H.-H., Huang, M.-H., Tsai, V. C., Chuang, R. Y., Feng, K.-F., and Lin, S.-H. Evidence for Fluid Migration During the 2016 Meinong, Taiwan, Aftershock Sequence. *Journal of Geophysical Research: Solid Earth*, 125(9), 2020. doi: 10.1029/2020jb019994.

Huber, P. J. Robust Regression: Asymptotics, Conjectures and Monte Carlo. *The Annals of Statistics*, 1(5):799–821, 1973.

Hunter, J. D. Matplotlib: A 2D graphics environment. *Computing in Science & Engineering*, 9(3):90–95, 2007. doi: 10.1109/MCSE.2007.55.

Igonin, N., Verdon, J. P., Kendall, J.-M., and Eaton, D. W. Large-Scale Fracture Systems Are Permeable Pathways for Fault Activation During Hydraulic Fracturing. *Journal of Geophysical Research: Solid Earth*, 126(3), 2021. doi: 10.1029/2020jb020311.

Jarvis, A., Reuter, H., Nelson, A., and Guevara, E. Hole-Filled Seamless SRTM Data V4: International Centre for Tropical Agriculture (CIAT). http://srtm.csi.cgiar.org, 2008.

Kennett, B. L. N. and Engdahl, E. R. Traveltimes for global earthquake location and phase identification. *Geophysical Journal International*, 105(2):429–465, may 1991. doi: 10.1111/j.1365-246x.1991.tb06724.x.

Keranen, K. M. and Weingarten, M. Induced Seismicity. *Annual Review of Earth and Planetary Sciences*, 46(1):149–174, 2018. doi: 10.1146/annurev-earth-082517-010054.

Kettlety, T., Verdon, J. P., Werner, M. J., and Kendall, J. M. Stress Transfer From Opening Hydraulic Fractures Controls the Distribution of Induced Seismicity. *Journal of Geophysical Research: Solid Earth*, 125(1), 2020. doi: 10.1029/2019jb018794.

Lecocq, T., Caudron, C., and Brenguier, F. MSNoise, a Python Package for Monitoring Seismic Velocity Changes Using Ambient Seismic Noise. *Seismological Research Letters*, 85(3):715–726, 2014. doi: 10.1785/0220130073.

Lin, G. Spatiotemporal variations of in situ V_p/V_s ratio within the Salton Sea Geothermal Field, southern California. *Geothermics*, 84:101740, 2020. doi: 10.1016/j.geothermics.2019.101740.

Lin, G. and Shearer, P. M. Estimating Local V_p/V_s Ratios within Similar Earthquake Clusters. *Bulletin of the Seismological Society of America*, 97(2):379–388, 2007. doi: 10.1785/0120060115.

Lin, G. and Shearer, P. M. Spatiotemporal Variations of Focal Mechanism and In Situ V_p/V_s Ratio During the 2018 Kīlauea Eruption. *Geophysical Research Letters*, 48(18), 2021. doi: 10.1029/2021gl094636.

Liu, T., Gong, J., Fan, W., and Lin, G. *In-situ* V_p/V_s ratio reveals fault-zone material variation at the westernmost Gofar transform fault, East Pacific Rise. *Journal of Geophysical Research: Solid Earth*, 128(3), 2023. doi: 10.1029/2022jb025310.

McNutt, S. R. Volcanic Seismology. *Annual Review of Earth and Planetary Sciences*, 33(1):461–491, 2005. doi: 10.1146/annurev.earth.33.092203.122459.

Mesimeri, M., Ganas, A., and Pankow, K. L. Multisegment ruptures and V_p/V_s variations during the 2020–2021 seismic crisis in western Corinth Gulf, Greece. *Geophysical Journal International*, 230(1):334–348, 2022. doi: 10.1093/gji/ggac081.

Nanometrics Inc. BCER Kiskatinaw Seismic Monitoring and Mit-

igation Area Velocity Model developed by Nanometrics Inc. https://www.bc-er.ca/data-reports/data-centre/, May 2020.

Natural Resources Canada. Earthquakes Canada, GSC, Earthquake Search (On-line Bulletin). https://earthquakescanada.nrcan.gc.ca/stndon/NEDB-BNDS/bulletin-en.php, 2023. https://earthquakescanada.nrcan.gc.ca/stndon/NEDB-BNDS/bulletin-en.php. (Date accessed: 2023-02-09).

Norgard, G. T. Structural inversion of the Middle Triassic Halfway Formation, Monias Field, northeast British Columbia. *Bulletin of Canadian Petroleum Geology*, 45(4):614–623, 1997. doi: 10.35767/gscpgbull.45.4.614.

Omovie, S. J. and Castagna, J. P. Relationships between Dynamic Elastic Moduli in Shale Reservoirs. *Energies*, 13(22):6001, 2020. doi: 10.3390/en13226001.

Peña Castro, A. F., Roth, M. P., Verdecchia, A., Onwuemeka, J., Liu, Y., Harrington, R. M., Zhang, Y., and Kao, H. Stress Chatter via Fluid Flow and Fault Slip in a Hydraulic Fracturing-Induced Earthquake Sequence in the Montney Formation, British Columbia. *Geophysical Research Letters*, 47(14), 2020. doi: 10.1029/2020gl087254.

Peterie, S. L., Miller, R. D., Intfen, J. W., and Gonzales, J. B. Earthquakes in Kansas Induced by Extremely Far-Field Pressure Diffusion. *Geophysical Research Letters*, 45(3):1395–1401, 2018. doi: https://doi.org/10.1002/2017GL076334.

Pimienta, L., Schubnel, A., Violay, M., Fortin, J., Guéguen, Y., and Lyon-Caen, H. Anomalous V_p/V_s Ratios at Seismic Frequencies Might Evidence Highly Damaged Rocks in Subduction Zones. *Geophysical Research Letters*, 45(22):12,210–12,217, 2018. doi: 10.1029/2018gl080132.

QGIS Development Team. *QGIS Geographic Information System 3.22.3*. QGIS Association, 2022. https://www.qgis.org. https://www.qgis.org.

Reuss, A. Calculation of the flow limits of mixed crystals on the basis of the plasticity of monocrystals. *Z. Angew. Math. Mech*, 9: 49–58, 1929.

Roth, M. P., Verdecchia, A., Harrington, R. M., and Liu, Y. High-Resolution Imaging of Hydraulic-Fracturing-Induced Earthquake Clusters in the Dawson-Septimus Area, Northeast British Columbia, Canada. *Seismological Research Letters*, 91(5): 2744–2756, 2020. doi: 10.1785/0220200086.

Roth, M. P., Kemna, K. B., Harrington, R. M., and Liu, Y. Source Properties of Hydraulic-Fracturing-Induced Earthquakes in the Kiskatinaw Area, British Columbia, Canada. *Journal of Geophysical Research: Solid Earth*, 127(3), 2022. doi: 10.1029/2021jb022750.

Salvage, R. O. and Eaton, D. W. Unprecedented quiescence in resource development area allows detection of long-lived latent seismicity. *Solid Earth*, 12(3):765–783, 2021. doi: 10.5194/se-12-765-2021.

Schmid, F., Petersen, G., Hooft, E., Paulatto, M., Chrapkiewicz, K., Hensch, M., and Dahm, T. Heralds of Future Volcanism: Swarms of Microseismicity Beneath the Submarine Kolumbo Volcano Indicate Opening of Near-Vertical Fractures Exploited by Ascending Melts. *Geochemistry, Geophysics, Geosystems*, 23(7), 2022. doi: 10.1029/2022gc010420.

Schultz, R., Skoumal, R. J., Brudzinski, M. R., Eaton, D., Baptie, B., and Ellsworth, W. Hydraulic Fracturing-Induced Seismicity. *Reviews of Geophysics*, 58(3), 2020. doi: 10.1029/2019rg000695.

Takei, Y. Effect of pore geometry on V_p/V_s: From equilibrium geometry to crack. *Journal of Geophysical Research*, 107(B2), 2002. doi: 10.1029/2001jb000522.

Verdecchia, A., Cochran, E. S., and Harrington, R. M. Fluid-Earthquake and Earthquake-Earthquake Interactions in Southern Kansas, USA. *Journal of Geophysical Research: Solid Earth*, 126(3):e2020JB020384, 2021. doi: https://doi.org/10.1029/2020JB020384.

Voigt, W. *Lehrbuch der Kristallphysik:(mit Ausschluss der Kristalloptik)*, volume 34. BG Teubner, 1910.

Wang, B., Harrington, R. M., Liu, Y., Kao, H., and Yu, H. A Study on the Largest Hydraulic-Fracturing-Induced Earthquake in Canada: Observations and Static Stress-Drop Estimation. *Bulletin of the Seismological Society of America*, 110(5):2283–2294, 2020. doi: 10.1785/0120190261.

Wang, B., Verdecchia, A., Kao, H., Harrington, R. M., Liu, Y., and Yu, H. A Study on the Largest Hydraulic Fracturing Induced Earthquake in Canada: Numerical Modeling and Triggering Mechanism. *Bulletin of the Seismological Society of America*, 2021. doi: 10.1785/0120200251.

Wang, W., Savage, M. K., Yates, A., Zal, H. J., Webb, S., Boulton, C., Warren-Smith, E., Madley, M., Stern, T., Fry, B., Mochizuki, K., and Wallace, L. Temporal velocity variations in the northern Hikurangi margin and the relation to slow slip. *Earth and Planetary Science Letters*, 584:117443, 2022. doi: 10.1016/j.epsl.2022.117443.

Weber, B., Becker, J., Hanka, W., Heinloo, A., Hoffmann, M., Kraft, T., Pahlke, D., Reinhardt, J., Saul, J., and Thoms, H. SeisComP3 - Automatic and Interactive Real Time Data Processing. In *Geophysical Research Abstracts*, 2007.

Wessel, P., Luis, J. F., Uieda, L., Scharroo, R., Wobbe, F., Smith, W. H. F., and Tian, D. The Generic Mapping Tools Version 6. *Geochemistry, Geophysics, Geosystems*, 20(11):5556–5564, 2019. doi: 10.1029/2019gc008515.

Winkler, K. W. and Nur, A. Seismic attenuation: Effects of pore fluids and frictional-sliding. *GEOPHYSICS*, 47(1):1–15, 1982. doi: 10.1190/1.1441276.

Worthington, M. H. and Hudson, J. A. Fault properties from seismic Q. *Geophysical Journal International*, 143(3):937–944, 2000. doi: 10.1046/j.1365-246x.2000.00315.x.

Yu, H., Harrington, R. M., Liu, Y., and Wang, B. Induced Seismicity Driven by Fluid Diffusion Revealed by a Near-Field Hydraulic Stimulation Monitoring Array in the Montney Basin, British Columbia. *Journal of Geophysical Research: Solid Earth*, 124, 2019. doi: 10.1029/2018JB017039.

Yu, H., Harrington, R. M., Kao, H., Liu, Y., Abercrombie, R. E., and Wang, B. Well Proximity Governing Stress Drop Variation and Seismic Attenuation Associated With Hydraulic Fracturing Induced Earthquakes. *Journal of Geophysical Research: Solid Earth*, 125(9), 2020. doi: 10.1029/2020jb020103.

Yu, H., Harrington, R. M., Kao, H., Liu, Y., and Wang, B. Fluid-injection-induced earthquakes characterized by hybrid-frequency waveforms manifest the transition from aseismic to seismic slip. *Nature Communications*, 12(1), 2021. doi: 10.1038/s41467-021-26961-x.

Zhao, D., Kanamori, H., Negishi, H., and Wiens, D. Tomography of the Source Area of the 1995 Kobe Earthquake: Evidence for Fluids at the Hypocenter? *Science*, 274(5294):1891–1894, 1996. doi: 10.1126/science.274.5294.1891.